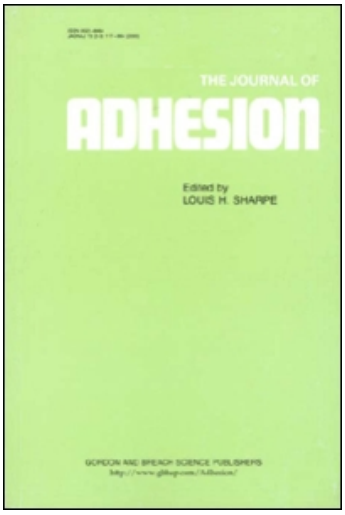

The Journal of Adhesion
Publication details, including instructions for authors and subscription information:
http://www.informaworld.com/smpp/title~content=t713453635

A Comparison of Several Fracture Mechanics Methods for Measuring Interfacial Toughness with Microbond Tests

R. J. Scheer[ab]; J. A. Nairn[a]
[a] Materials Science and Engineering, University of Utah, Salt Lake City, Utah, USA [b] Protein Solutions. Inc., Salt Lake City, Utah, USA

To cite this Article Scheer, R. J. and Nairn, J. A.(1995) 'A Comparison of Several Fracture Mechanics Methods for Measuring Interfacial Toughness with Microbond Tests', The Journal of Adhesion, 53: 1, 45 — 68
To link to this Article: DOI: 10.1080/00218469508014371
URL: http://dx.doi.org/10.1080/00218469508014371

J. Adhesion, 1995, Vol. 53, pp. 45–68
Reprints available directly from the publisher
Photocopying permitted by license only

A Comparison of Several Fracture Mechanics Methods for Measuring Interfacial Toughness with Microbond Tests*

R. J. SCHEER** and J. A. NAIRN†

Materials Science and Engineering, University of Utah, Salt Lake City, Utah 84112, USA

(Received October 22, 1994; in final form February 15, 1995)

Several stress analysis methods were used to find the energy release rate for initiation of an interfacial crack in a microbond specimen. First, we used a recently-derived variational mechanics analysis of the stresses in a microbond specimen. Previous studies for analysis of crack growth have used shear-lag methods. For a second analysis, we present a new, and more complete, shear-lag analysis of the microbond specimen. Third, we consider some previously-published theories. For each of the stress analyses, the calculated energy release rate was used to predict the debonding stress as a function of the droplet length. The predictions were compared with two experimental results. Our new analyses that include residual thermal stresses were found to be the best. It was further observed that some of the terms in the analysis are negligible. The remaining terms provide a simple tool for doing a fracture mechanics analysis of microbond experiments.

KEYWORDS: microbond test; interface; interface toughness; fracture mechanics; composites; residual stresses

1 INTRODUCTION

Many researchers have used model single fiber composites to study the fiber/matrix interface. A recently-developed single fiber technique, the microbond test, has been shown to be a reproducible and relatively simple test method.[1–7] Figure 1A shows a schematic view of the microbond test. The fiber is threaded between a vice or two knife edges and pulled. The knife edges contact the matrix droplet eventually shearing off the droplet when the load on the fiber gets to the debond load for the specimen. The experimental data are the debond load and the specimen geometry (*i.e.*, fiber radius, droplet diameter, and droplet length). Our goal was to develop a new method for interpreting experimental microbond test data.

* One of a Collection of papers honoring Lawrence T. Drzal, the recipient in February 1994 of *The Adhesion Society Award for Excellence in Adhesion Science, Sponsored by* 3 *M*.

** Present address: Protein Solutions, Inc., 350 West 800 North, Suite 218, Salt Lake City, Utah 84103, USA.

† Corresponding author.

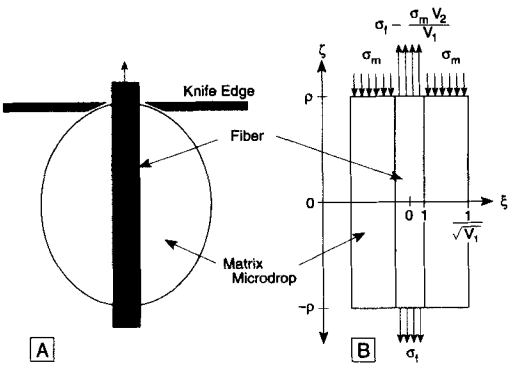

FIGURE 1 A microbond specimen of dimensionless length, 2ρ, showing the actual specimen, (A), and an idealized cylindrical model, (B), under test loading conditions. σ_f is the background fiber tensile stress or the stress on the fiber due to weight of the fiber below the droplet. σ_m is the stress applied to the droplet during the test. ξ and ζ represent the dimensionless radial and axial coordinates, respectively. The stresses on the top of the fiber and matrix cylinders are balanced with the σ_f stress on the bottom of the fiber. The net axial stress on any cross-section is $\sigma_0 = V_1\sigma_f$ where V_1 is the volume fraction of the fiber.

A recent study has concluded that a critical energy release rate for interfacial crack growth failure criterion is more accurate than either an average shear[1] or total energy[8] failure criterion in predicting the failure load of microbond specimens.[8,9] In this study, a recently-derived variational mechanics analysis,[8] a new shear-lag analysis, two existing shear-lag analyses, and a simple limiting model for long droplet lengths are all used to calculate the energy release rate for growth of an interfacial crack in the microbond specimen. By assuming that debonding occurs when the energy release rate reaches a critical energy release rate, denoted as G_{ic}, we predicted debond force as a function of droplet length for all theories. The predictions were compared with our own experimental results and with some literature experimental results.

2 MATERIALS AND METHODS

Microbond specimens were prepared by placing a microscopic droplet of epoxy resin (diameter 20–200 μm) on a fiber and curing the droplet by following vendor-recommended procedures. To aid in specimen positioning, a larger "marker" drop was also cured on the fiber at a measured distance from the droplet to be tested. Sample measurements of droplet diameter, droplet length, and distance between the droplet and marker drop were recorded for each spcimen (see Fig. 2). The specimens were then placed in the microbond jig (see Fig. 3) and the fibers were translated upward at a steady rate while the droplet was held in place by means of two microvise grips. The droplet was continually observed through a telescope to confirm a clean and complete debond event. During the debond procedure, the load on the fiber was recorded by computer. Only data from axisymmetric-shaped droplets that generated complete and clean debond events were used for subsequent analysis.

In order to facilitate the difficult handling of specimens with fragile fibers, each fiber to be tested was mounted on a cardboard specimen holder. The as-received yarns were

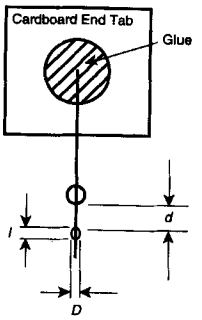

FIGURE 2 Schematic diagram showing the experimental parameters of droplet length, *l*, droplet diameter, *D*, and marker distance, *d*.

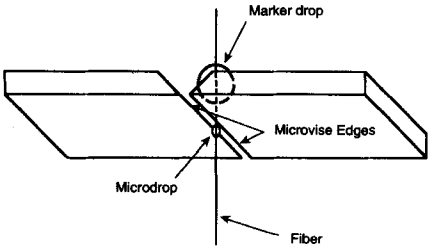

FIGURE 3 The microbond testing jig showing the microvise and the fiber. The fiber has a droplet which is sheared off by the microvise and a marker drop that was used to aid in positioning the droplet within the microvise.

cut with a razor into lengths of approximately 5 cm and stored in covered containers. Individual fibers were then removed from the yarns, placed on cardboard sample holders and secured with a small drop of Elmer's Glue-All® placed at each end of the fiber (see Fig. 2).

The matrix material was EPON 828® which consists of a diglycidylether of bisphenol A (DGEBA) liquid epoxy resin, and meta-phenylenediamine (MPDA), an amine curing agent. DGEBA and MPDA were purchased from Shell Chemical Company and Aldrich Chemical Company, respectively. The recommended stoichiometric ratio to ensure complete curing is 16 parts MPDA to 100 parts resin by weight.[10] Some physical properties of cured EPON 828 are listed in Table I. The epoxy droplets were cured on the fibers at 75°C for 2 hours and at 125°C for 3 hours.

Our experiments used E-glass fibers (obtained from Owens-Corning Fiberglass in Toledo, Ohio) with a diameter of 21 μm. The literature data we analyzed used Kevlar® 49 aramid fibers (obtained from DuPont in Wilmington, Delaware). Table I summarizes some physical properties of these fibers. The E-glass fibers were used in their as-received state and care was taken not to contaminate the fiber surfaces with oils, dust, or solvents. To insure surface purity all fibers were handled with clean tweezers and stored in separate covered containers.

TABLE I

Mechanical and thermal properties of the fibers and matrix used in this paper and linear fitting parameters for predicting droplet diameter as a function of length. The transverse and shear properties of Kevlar® 49 aramid fibers are difficult to determine. The numbers in this table are estimates. Fortunately, the precise values of these specific properties do not strongly affect the calculated energy release rates

Property	E-Glass	Kevlar® 49	Epon 828
Diameter ($2r_1$)(μm)	21	11.7	
Tensile Modulus (E_A or E_m) (GPa)	75	130	3.3
Transverse Modulus (E_T) (GPa)	75	10	
Axial Shear Modulus (G_A or G_m) (GPa)	32	15	1.23
Axial Poisson's Ratio (ν_A or ν_m)	0.17	0.2	0.35
Transverse Poisson's Ratio (ν_T)	0.17	0.35	
Axial CTE (α_A or α_m) (ppm/°C)	5	−2	48
Transverse CTE (α_T) (ppm/°C)	5	60	
Diameter *vs.* Length Slope (A)	0.878	0.943	
Diameter *vs.* Length Intercept (B) (μm)	−40.6	−33.2	

3 STRESS ANALYSIS AND ENERGY RELEASE RATE

3.1 Variational Mechanics Stress Analysis

The idealized specimen in Figure 1B was the specimen used for all stress analyses. Instead of an ellipsoidal droplet, the droplet was assumed to be a cylinder on the fiber. Instead of point loading by knife edges, the load was assumed to be applied uniformly over the top of the matrix cylinder. In Ref. 8, the idealized microbond specimen with droplet length, l (and axial ratio $\rho = l/2r_1$), was analyzed by making only one assumption–that the axial stresses in the fiber and in the matrix cylinders depend only on the axial coordinate (z) and are independent of the radial coordinate (r), all stresses in the matrix and cylinder can be written in terms of a single unknown function, $\psi(\zeta)$, where $\zeta = z/r_1$ is a dimensionless axial coordinate normalized to the fiber radius, r_1. The stresses in the fiber are

$$\sigma_{zz,1} = \psi \tag{1}$$

$$\tau_{rz,1} = -\frac{\xi\psi'}{2} \tag{2}$$

$$\sigma_{rr,1} = \frac{\psi''}{16}\left(\xi^2(3+\nu_T) + \nu_m - \nu_T + \frac{2(1+\nu_m)\ln V_1}{V_2} - \frac{V_2 A_1}{V_1 A_0}\right) - \frac{V_2}{V_1}\left(\frac{A_3\psi + A_4\sigma_0 + A_5\Delta T}{A_0}\right) \tag{3}$$

$$\sigma_{\theta\theta,1} = \frac{\psi''}{16}\left(\xi^2(1+3\nu_T) + \nu_m - \nu_T + \frac{2(1+\nu_m)\ln V_1}{V_2} - \frac{V_2 A_1}{V_1 A_0}\right) - \frac{V_2}{V_1}\left(\frac{A_3\psi + A_4\sigma_0 + A_5\Delta T}{A_0}\right) \tag{4}$$

The stresses in the matrix are

$$\sigma_{zz,2} = \frac{\sigma_0}{V_2} - \frac{V_1\psi}{V_2} \tag{5}$$

$$\tau_{rz,2} = \frac{V_1\psi'}{2V_2}\left(\xi - \frac{1}{\xi V_1}\right) \tag{6}$$

$$\sigma_{rr,2} = \frac{\psi''}{16V_2}\left[(3+\nu_m)(1-\xi^2V_1) + 2(1+\nu_m)\ln\xi^2V_1 + \frac{V_2A_1}{A_0}\left(1-\frac{1}{\xi^2V_1}\right)\right] + \left(1-\frac{1}{\xi^2V_1}\right)\left(\frac{A_3\psi + A_4\sigma_0 + A_5\Delta T}{A_0}\right) \tag{7}$$

$$\sigma_{\theta\theta,2} = \frac{\psi''}{16V_2}\left[(1+3\nu_m)(1-\xi^2V_1) - 2(1-\nu_m) + 2(1+\nu_m)\ln\xi^2V_1 + \frac{V_2A_1}{A_0}\left(1+\frac{1}{\xi^2V_1}\right)\right] + \left(1+\frac{1}{\xi^2V_1}\right)\left(\frac{A_3\psi + A_4\sigma_0 + A_5\Delta T}{A_0}\right) \tag{8}$$

In these equations the subscripts 1 and 2 refer to the fiber and matrix cylinders, respectively, ν_m is the Poisson's ratio of the isotropic matrix, ν_T is the transverse Poisson's ratio of the transversely isotropic fiber, V_1 and V_2 are the volume fractions of the fiber and the matrix, A_1 to A_5 are material- and geometry-specific constants (see Appendix), σ_0 is the total stress applied in the z direction ($\sigma_0 = V_1\sigma_f$ where σ_f is the background tensile stress–see Fig. 1), ΔT is the difference between the stress-free temperature and the specimen temperature, and ξ is a dimensionless radial coordinate defined by $\xi = r/r_1$. By axisymmetry, the unspecified shear stresses are all zero. (Note: Eqs. (7) and (8) correct a misprint in Ref. 8 and follows the originally-correct equations in Ref. 11).

The stresses in Equations (1)–(8) constitute an admissible stress state. By the principles of variational mechanics, the best approximation to the true stress state is found by finding the $\psi(\zeta)$ that minimizes the total complementary strain energy. The solution to the minimization problem presented in Ref. 8 is written as

$$\psi(\zeta) = \psi_0 - \phi(\zeta) \tag{9}$$

where ψ_0 is a constant defined by

$$\psi_0 = -\frac{C_{13}\sigma_0 + D_3\Delta T}{C_{33}} \tag{10}$$

and $\phi(\zeta)$ is the solution to the homogeneous, fourth-order differential equation

$$\frac{d^4\phi(\zeta)}{d\zeta^4} + p\frac{d^2\phi(\zeta)}{d\zeta^2} + q\phi(\zeta) = 0 \tag{11}$$

In these equations, C_{ij}, D_i, p and q depend only on mechanical properties of the fiber and matrix and on the geometry of the specimen; they are defined in the Appendix. Physically, the constant ψ_0 is the far-field fiber stress or the stress that would exist in the fiber far from the ends of an infinitely-long droplet.

From Figure 1B and the stresses in Equations (1)–(8), the boundary conditions on $\phi(\zeta)$ at $\pm\rho$ are

$$\phi(\rho)=\psi_0-\frac{\sigma_0-\sigma_m V_2}{V_1}\quad \phi(-\rho)=\psi_0-\frac{\sigma_0}{V_1}\quad \phi'(\pm\rho)=0 \tag{12}$$

Using these boundary conditions, the solution to Equation (11) can be expressed as

$$\phi(\zeta)=\left(\psi_0-\frac{\sigma_0}{V_1}+\frac{\sigma_m V_2}{2V_1}\right)\phi_e(\zeta)+\left(\frac{\sigma_m V_2}{2V_1}\right)\phi_0(\zeta) \tag{13}$$

where $\phi_e(\zeta)$ and $\phi_0(\zeta)$ are even and odd functions of ζ; they are defined in the Appendix.

For energy release rate calculations, we need to calculate the total strain energy in the microbond specimen. Using the stresses in Equations (1)–(8) to find the strain energy and integrating over the volume of the specimen gives the total strain energy. From calculations in Ref. 8, the strain energy integral simplifies to

$$U(\rho)=\pi r_1^3\int_{-\rho}^{\rho} d\zeta(C_{33}\psi^2+2C_{35}\psi\psi''+C_{55}\psi''^2+C_{44}\psi'^2) \tag{14}$$

(Note: the r_1^3 in Eq. (14) corrects a misprint in the corresponding equation in Ref. 8 which had r_1^2). In Equation (14), we have assumed that $\sigma_f=\sigma_0=0$. This assumption follows the typical microbond experiment[1] in which the background fiber stress, σ_f, is negligible. Eliminating σ_f leads to considerable simplification. If subsequent experiments show that σ_f is an important variable, the variational mechanics analysis can include its effects by rederiving the strain energy for non-zero σ_f (see Ref. 8). Substituting the known function $\psi(\zeta)$ and integrating gives:[8]

$$U(\rho)=2C_{55}\rho\pi r_1^3\left[\frac{D_3^2\Delta T^2}{C_{33}^2}\left(\frac{C_{33}}{C_{55}}-\frac{\chi_e(\rho)}{\rho}\right)+\left(\frac{\sigma_m V_2}{2V_1}\right)^2\left(\frac{\chi_e(\rho)+\chi_0(\rho)}{\rho}\right)\right] \tag{15}$$

where the new constant C_{55} and the new functions $\chi_e(\rho)$ and $\chi_0(\rho)$ are defined in the Appendix.

3.2 New Shear-Lag Stress Analysis

The shear-lag model or Cox analysis[12] is commonly used to analyze stress transfer from the fiber to the matrix.[12-17] Here we present a new shear-lag treatment of the microbond specimen and cast it in a form analogous to the above variational mechanics analysis. By the shear-lag assumption, the rate of change in axial load in the fiber is given by[12]

$$\frac{dP}{dz}=2\pi r_1\tau=H(u-v) \tag{16}$$

where P is the axial load in the fiber, τ is the interfacial shear stress, H is a shear-lag parameter, u is the fiber displacement, and v is the matrix displacement in the absence of the fiber (*i.e.*, the far-field displacement). If we convert the load to stress, differentiate with respect to z, and express the equation in the dimensionless ζ coordinate, Equation (16) becomes

$$\frac{d^2\psi_s(\zeta)}{d\zeta^2}-\omega^2\psi_s(\zeta)=-\omega^2\psi_{0s} \tag{17}$$

where $\psi_s(\zeta)$ is the average axial stress in the fiber (it is analogous to $\psi(\zeta)$ in the variational mechanics analysis), ω is a shear-lag parameter ($\omega = \sqrt{H/\pi E_A}$), and ψ_{0s} is the far-field stress in the fiber (it is analogous to ψ_0 in the variational mechanics analysis). By a simple one-dimensional, thermal-elastic analysis of an infinitely-long fiber in a matrix where the fiber and matrix have equal axial strains, it is easy to find ψ_{0s}. Casting the result in the form of Equation (10) gives

$$\psi_{0s} = -\frac{C_{13s}\sigma_0 + D_{3s}\Delta T}{C_{33s}} \tag{18}$$

where the shear-lag constants (C_{13s}, C_{33s}, and D_{3s}) are defined in the Appendix.

Continuing the analogy with the variational mechanics analysis, we write

$$\psi_s(\zeta) = \psi_{0s} - \phi_s(\zeta) \tag{19}$$

where $\phi_s(\zeta)$ is the solution to the homogeneous, second-order differential equation

$$\frac{d^2\phi_s(\zeta)}{d\zeta^2} - \omega^2\phi_s(\zeta) = 0 \tag{20}$$

with boundary conditions

$$\phi_s(\rho) = \psi_{0s} - \frac{\sigma_0 - \sigma_m V_2}{V_1} \quad \phi(-\rho) = \psi_{0s} - \frac{\sigma_0}{V_1} \tag{21}$$

Equation (20) is easy to solve. Using the form of the variational mechanics analysis, the solution is

$$\phi_s(\zeta) = \left(\psi_{0s} - \frac{\sigma_0}{V_1} + \frac{\sigma_m V_2}{2V_1}\right)\phi_{es}(\zeta) + \left(\frac{\sigma_m V_2}{2V_1}\right)\phi_{0s}(\zeta) \tag{22}$$

where $\phi_{es}(\zeta)$ and $\phi_{0s}(\zeta)$ are even and odd functions of ζ; they are defined in the Appendix.

Although shear-lag analyses are normally only derived to give the axial stress in the fiber and the interfacial shear stress,[16] use of stress equilibrium allows one to calculate axial stresses and shear stresses at any position. The analysis is a one-dimensional analogue of the variational mechanics analysis. The shear stresses that result from the already-determined tensile stresses are analogous to the stresses in Equations (1)–(8). Thus, the shear-lag stresses in the fiber and matrix are

$$\sigma_{zz,1} = \psi_s, \tag{23}$$

$$\tau_{rz,1} = -\frac{\xi\psi_s'}{2} \tag{24}$$

$$\sigma_{zz,2} = \frac{\sigma_0}{V_2} - \frac{V_1\psi_s}{V_2} \tag{25}$$

$$\tau_{rz,2} = \frac{V_1\psi_s'}{2V_2}\left(\xi - \frac{1}{\xi V_1}\right) \tag{26}$$

The transverse stresses (σ_{rr} and $\sigma_{\theta\theta}$) are zero, or rather undetermined, because the shear-lag analysis is a one-dimensional analysis. By axisymmetry, the unspecified shear stresses are zero. For total strain energy, we can either directly integrate the strain energy, or use Equation (14) and drop terms involving the transverse stresses.[8] The

resulting total strain energy by the shear lag analysis when $\sigma_f = \sigma_0 = 0$ becomes

$$U_s(\rho) = \pi r_1^3 \int_{-\rho}^{\rho} d\zeta (C_{33s}\psi_s^2 + C_{44}\psi_s'^2) \tag{27}$$

Substituting the known function $\psi_s(\zeta)$ and integrating gives:

$$U_s(\rho) = 2C_{55s}\rho\pi r_1^3 \left\{ \frac{D_{3s}^2 \Delta T^2}{C_{33s}^2} \left[\frac{C_{33s}}{C_{55s}} \left(1 - \frac{\tanh \omega\rho}{\omega\rho} \right) + \frac{\chi_a(\rho)}{\rho} \right] - \frac{D_{3s}\Delta T \sigma_m V_2}{C_{33s} V_1} \frac{\chi_a(\rho)}{\rho} \right.$$
$$\left. + \left(\frac{\sigma_m V_2}{2V_1} \right)^2 \left[\frac{C_{33s}}{C_{55s}} \left(\frac{2\coth 2\omega\rho}{\omega\rho} \right) + \frac{\chi_a(\rho) + \chi_b(\rho)}{\rho} \right] \right\} \tag{28}$$

where the new constant, C_{55s}, and the new functions, $\chi_a(\rho)$ and $\chi_b(\rho)$, are defined in the Appendix.

3.3 Energy Release Rate Analysis

The most widely used approach for analyzing failure in microbond specimens is to assume that the droplet shears off the fiber when the *average* shear stress at the interface, $\langle \tau_{rz}(\xi = 1) \rangle$, reaches the interfacial shear strength, τ_{ic}. By integrating the equations of stress equilibrium it is possible to derive an exact relation between $\langle \tau_{rz}(\xi = 1) \rangle$ and fiber force, F:

$$\langle \tau_{rz}(\xi = 1) \rangle = \frac{F}{2\pi r_1 l} \tag{29}$$

The force, F_d, or the stress, $\sigma_d = -\sigma_m V_2 / V_1$, in the fiber at the instant of debonding as a function of droplet length are thus predicted to be linear:

$$F_d = 2\pi r_1 l \tau_{ic} \quad \text{or} \quad \sigma_d = 4\tau_{ic}\rho \tag{30}$$

There are two problems with Equation (30). First, it is in poor agreement with experimental data over a wide range of droplet lengths. Results presented later in this paper and results in other publications[2,5,9] show that debond stress is not linear in ρ, but rather levels off at large ρ. Second, despite the fact that Equation (29) is an exact expression of stress equilibrium, the assumption that average shear stress determines failure is unrealistic. A variational stress analysis[8] or a finite element analysis[18] show that the shear stress is nonuniform and that there is a significant radial tensile stress concentration at the point where the fiber enters the droplet. It is probably incorrect to ignore these features of the stress state and to attribute failure only to the level of average interfacial shear stress.

In Ref. 8, we proposed several alternative failure criteria. In this paper, we discuss a fracture mechanics method where debonding is predicted based on the energy release rate for initiation of an interfacial crack. The highest interfacial stresses are at the point where the matrix is contacted by the microvise (see $\zeta = +\rho$ in Fig. 1). It is, therefore, logical to assume that debonding will be caused by initiation of an interfacial crack at $\zeta = +\rho$. This assumption agrees with experimental observations of microbond failures.[17] In this section we use the variational mechanics stress analysis and the shear-lag stress analysis to calculate the energy release rate for initiation of an interfacial

crack–G_i. By assuming that specimen failure occurs when G_i reaches the critical energy release rate for the interface, or the interfacial toughness, G_{ic}, we further predict σ_d as a function of droplet length.

For a crack propagation analysis, we must consider a microbond specimen with an interfacial crack. Figure 4 shows an idealized microbond specimen with a crack of length a or dimensionless length 2δ where $\delta = a/2r_1$. The specimen is now divided into two regions–region I is the region within the interfacial crack and region II is the region with an intact interface. Our first step is to find the stresses and strain energies in each region. We begin by using the variational mechanics analysis.

Because the interfacial radial stress is tensile before crack formation,[8] we assume the crack in Figure 4 opens and that the crack surfaces are stress-free. The only possible stress state in region I in which σ_{zz} is independent of r is simple uniaxial tension. When σ_f is negligible, the axial stresses in the fiber and matrix are

$$\sigma_{zz,1} = -\frac{\sigma_m V_2}{V_1} \quad \text{and} \quad \sigma_{zz,2} = \sigma_m \tag{31}$$

All other stresses are zero. The total strain energy in region I is

$$U_1(\delta) = 2\delta\pi r_1^3\left[\frac{\sigma_m^2 V_2}{2V_1}\left(\frac{V_2}{V_1 E_A} + \frac{1}{E_m}\right)\right] = 2\delta\pi r_1^2 C_{33s}\sigma_d^2 \tag{32}$$

The stresses at the top of region II are determined by the stresses in region I. From Equation (31) the stresses at the top of region II are identical to the boundary conditions in Equation (12) when $\sigma_0 = 0$. Thus, the stresses and strain energy in region II are the stresses and strain energy that exist is a microbond specimen of dimensionless length $2(\rho - \delta)$, or $U_{II}(\delta) = U(\rho - \delta)$. The total strain energy in the cracked microbond specimen is

$$U_c(\rho, \delta) = U_I(\delta) + U(\rho - \delta) \tag{33}$$

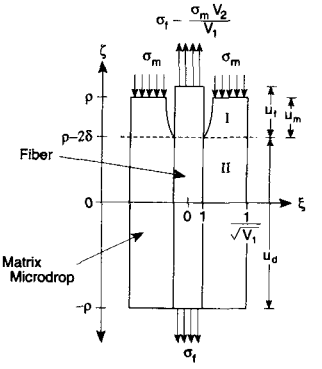

FIGURE 4 An idealized microbond specimen of dimensionless length, 2ρ, having an interfacial crack of dimensionless length, 2δ, emanating from the top of the droplet. Region I is the cracked region above the dashed line. Region II is the uncracked region below the dashed line.

The total energy release rate associated with growth of the crack in Figure 4 is[19]

$$G_i = \frac{\partial W}{\partial A} - \frac{\partial U_c}{\partial A} = \frac{\partial W}{\partial A} - \frac{\partial U_1(\delta)}{\partial A} - \frac{\partial U(\rho - \delta)}{\partial A} \tag{34}$$

where W is external work and $A = 2\pi r_1 a = 4\pi r_1^2 \delta$ is total crack area. We consider the knife edges as fixed and σ_f as negligible. When the debond extends, the only external work is the work done by the fiber stresses which is expended through the distance $u_f - u_m$ (see Fig. 4). Thus,

$$\frac{\partial W}{\partial A} = \frac{1}{4\pi r_1^2}\frac{\partial W}{\partial \delta} = \frac{\sigma_d}{4}\frac{\partial (u_f - u_m)}{\partial \delta} \tag{35}$$

By integrating the strains in region I (including thermal strains), the relevant displacement difference is

$$u_f - u_m = 4\delta r_1 (D_{3s}\Delta T + C_{33s}\sigma_d) \tag{36}$$

Evaluating

$$\frac{\partial W}{\partial A} = r_1(D_{3s}\sigma_d \Delta T + C_{33s}\sigma_d^2) \quad \text{and} \quad \frac{\partial U_I}{\partial A} = \frac{1}{4\pi r_1^2}\frac{\partial U_I}{\partial \delta} = \frac{r_1}{2} C_{33s}\sigma_d^2 \tag{37}$$

and substituting into Equation (34) gives

$$G_i(\delta) = \frac{r_1}{2}\left[C_{33s}\sigma_d^2 + 2D_{3s}\sigma_d \Delta T - \frac{1}{2\pi r_1^3}\frac{\partial U(\rho - \delta)}{\partial \delta} \right] \tag{38}$$

Substituting the variational mechanics strain energy in Equation (15) into Equation (38), and evaluating the derivatives at $\delta = 0$ gives the energy release rate for the initiation of interfacial debonding:

$$G_i(0) = \frac{r_1}{2}\left\{ C_{33s}\sigma_d^2 + 2D_{3s}\sigma_d \Delta T + C_{55}\left[\frac{D_3^2 \Delta T^2}{C_{33}^2}\left(\frac{C_{33}}{C_{55}} - \chi_e'(\rho) \right) + \frac{\sigma_d^2}{4}(\chi_e'(\rho) + \chi_0'(\rho)) \right] \right\} \tag{39}$$

The required derivatives of $\chi_e(\rho)$ and $\chi_0(\rho)$ are given in the Appendix. The only difference when calculating the energy release rate using the new shear-lag analysis is that $U(\rho - \delta)$ in Equation (38) must be replaced by $U_s(\rho - \delta)$. Substituting Equation (28) into Equation (38) gives

$$G_{is}(0) = \frac{r_1}{2}\left\{ C_{33s}\sigma_d^2 + 2D_{3s}\sigma_d \Delta T + C_{55s}\left[\frac{D_{3s}^2 \Delta T^2}{C_{33s}^2}\left(\frac{C_{33s}}{C_{55s}} \tanh^2 \omega\rho + \chi_a'(\rho) \right) \right.\right.$$
$$\left.\left. + \frac{D_{3s}\sigma_d \Delta T}{C_{33s}}\chi_a'(\rho) + \frac{\sigma_d^2}{4}\left(\chi_a'(\rho) + \chi_b'(\rho) - \frac{4C_{33s}}{C_{55s}} \operatorname{csch}^2 2\omega\rho \right) \right] \right\} \tag{40}$$

The required derivatives of $\chi_a(\rho)$ and $\chi_b(\rho)$ are given in the Appendix.

Figure 5 plots the energy release rate calculated by variational mechanics, by the new shear-lag analysis, and by finite element analysis for initiation of an interfacial crack as a function of ρ. The plot in Figure 5 is for an E-glass fiber in an epoxy matrix with $V_1 = 0.10$. For the new shear-lag analysis we set the undetermined parameter, ω,

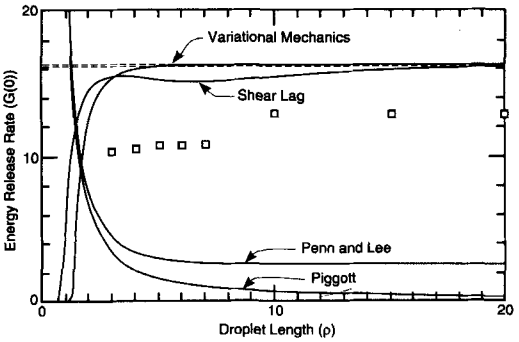

FIGURE 5 Energy release rate for initiation of an interfacial debond in microbond specimens as a function of the aspect ratio of the droplet. The energy release rate was calculated by various theories and by finite element analysis. The square symbols are the results from finite element analysis. The stress applied to the matrix was -30 MPa. The thermal load was $\Delta T = -100\,^{\circ}\mathrm{C}$. The fiber type was E-glass and the matrix was an epoxy.

according to the recommendations of Cox:[12]

$$\omega = \sqrt{\frac{2G_m}{E_A \ln \frac{r_2}{r_1}}} \tag{41}$$

where r_2 is the outer radius of the droplet. Typical microbond experiments have ρ values between 5 and 20. Over the range of 5 to 20 in Figure 5, the variational mechanics and shear-lag models agree within 10%. The range over which the two theories agree depends on V_1. At low V_1 (< 0.05) the two theories can differ significantly at low ρ. At higher V_1 (> 0.05) the two theories are generally within 10% over the entire range of experimental ρ's.

The two analytical solutions and the finite element analysis (symbols in Fig. 5) differ by about 20%. We claim this agreement to show the analytical solutions have reasonable accuracy. There is, however, no certainty that the finite element analyses gave the correct energy release rates. Finite element analysis of interfacial cracks is a difficult problem. The necessity of using several finite values for δ and extrapolating to $\delta = 0$ to find $G_i(0)$ compounds the problem. We used about 1500 degrees of freedom and crack-closure methods to find the results in Figure 5. The results, however, were sensitive to the mesh configuration and the δ's used for extrapolation. Finer meshes did not necessarily produce more accurate results. If the mesh was too fine, the crack-closure calculations would be unpredictably affected by oscillating stresses at the interfacial crack tip.[20] At short droplet lengths, the analytical solutions decreased rapidly while the finite element results did not. This expected result is caused by a breakdown of the assumption that the axial stresses are independent of r. This assumption is best for long slender droplets and breaks down for short aspect ratio droplets.[8] Fortunately, typical experimental droplets have $\rho > 5$.

The analytical solutions all give total energy release rate. The finite element analysis, however, can be partitioned into mode I and mode II energy release rates. This partitioning reveals that initiation of debonding is pure mode I fracture. This calculation is contrary to the simplistic view of the microbond test as shearing off the droplet

and, therefore, being a mode II fracture. The explanation is that before crack initiation there is a large tensile radial stress at $\zeta = +\rho$ and boundary conditions dictate that interfacial shear stress is zero. This stress state leads to mode I fracture. As the crack grows, the stress state changes and finite element analysis shows that the amount of mode II deformation increases. If debonding is controlled by the initiation of the interfacial crack, however, the microbond test should be considered as measuring the *tensile* or mode I failure properties of the interface and not the interfacial *shear* strength or mode II failure properties.

In the limit as $\rho \to \infty$, the energy release rate by variational mechanics (Eq. (39)), by shear lag (Eq. (40)), and by finite element analysis all become constant. Denoting the limiting value as $G_i^*(0)$, the variational mechanics theory gives

$$G_i^*(0) = \lim_{\rho\to\infty} G_i(0) = \frac{r_1}{2}\left(C_{33s}\sigma_d^2 + 2D_{3s}\sigma_d\Delta T + \frac{D_3^2\Delta T^2}{C_{33}}\right) \tag{42}$$

The limiting value for the shear lag analysis is the same except that D_3 and C_{33} in the last term are replaced by D_{3s} and C_{33s}. The limiting values for the variational mechanics and shear-lag analysis are plotted as dashed lines in Figure 5. Physically, the first two terms correspond to the work term and the change in strain energy in region I; they are identical to the first two terms in Equations (39) and (40). The last term is all that remains from the change in strain energy in region II. At the top of region II, there is a stress concentration. As the crack moves this stress concentration moves but, if the droplet is long, the stress concentration is unaltered and thus releases no strain energy. The strain energy in region II that is released is released from the opposite end or bottom of the droplet. If ρ is large, the bottom of the droplet is far away from the stress concentration and the stresses caused by σ_d will be negligible. The only strain energy remaining is the thermal strain energy. The last term in Equation (42) is thus the amount of thermal strain energy released as crack growth causes region II to become shorter.

As long as V_1 is not too large, $G_i(0)$ will reach its limiting value of $G_i^*(0)$ quickly. Figure 5 shows $G_i^*(0)$ is very close to the full $G_i(0)$ for ρ in the range of 5 to 20. Many experimental results fall within this range and, thus, we have the potential of analyzing them using the simpler result in Equation (42) rather than the more detailed results in Equations (39) and (40). When using Equation (42) we only have to determine the constants D_3, C_{33}, D_{3s}, and C_{33s}. For the shear-lag analysis, we further note that Equation (42) does not depend on the unknown shear-lag parameter ω.

We assumed microbond specimens debond when the energy release rate for crack initiation, $G_i(0)$, is equal to the interfacial fracture toughness, G_{ic}. This assumption implies that there is no initial debond ($\delta = 0$). There is still, however, a stress singularity at the bimaterial interface where the fiber enters the matrix; we are assuming that this singularity initiates the debonding. $G_i(0)$, $G_{is}(0)$ and $G_i^*(0)$ in Equations (39), (40) and (42) are each quadratic in σ_d. Solving the quadratic equations and taking the positive root gives

$$\sigma_d(\rho) = \frac{-b + \sqrt{b^2 - 4ac}}{2a} \tag{43}$$

where for the variational mechanics analysis

$$a = C_{33s} + \frac{C_{55}}{4}(\chi_e'(\rho) + \chi_0'(\rho)) \tag{44}$$

$$b = 2D_{3s}\Delta T \tag{45}$$

$$c = \frac{D_3^2 \Delta T^2}{C_{33}^2}(C_{33} - C_{55}\chi_e'(\rho)) - \frac{2G_{ic}}{r_1} \tag{46}$$

For the shear-lag analysis

$$a_s = C_{33s}(1 - \operatorname{csch}^2 2\omega\rho) + \frac{C_{55s}}{4}(\chi_a'(\rho) + \chi_b'(\rho)) \tag{47}$$

$$b_s = 2D_{3s}\Delta T + C_{55s}\frac{D_{3s}\Delta T}{C_{33s}}\chi_a'(\rho) \tag{48}$$

$$c_s = \frac{D_{3s}^2 \Delta T^2}{C_{33s}^2}(C_{33}\tanh^2\omega\rho + C_{55s}\chi_a'(\rho)) - \frac{2G_{ic}}{r_1} \tag{49}$$

where the subscript s has been added to denote shear-lag analysis. For the simple analysis in Equation (42)

$$\sigma_d(\rho) = -\frac{D_{3s}\Delta T}{C_{33s}} + \sqrt{\frac{2G_{ic}}{r_1 C_{33s}} + \frac{\Delta T^2}{C_{33s}}\left(\frac{D_{3s}^2}{C_{33s}} - \frac{D_3^2}{C_{33}}\right)} \tag{50}$$

for a variational analysis. For the shear-lag analysis, replace D_3 and C_{33} by D_{3s} and C_{33s} to get:

$$\sigma_d(\rho) = -\frac{D_{3s}\Delta T}{C_{33s}} + \sqrt{\frac{2G_{ic}}{r_1 C_{33s}}} \tag{51}$$

3.4 Other Shear-Lag Analyses

Several authors have combined shear-lag methods and fracture mechanics to predict interfacial debonding.[16,17,21] Here, we consider two analyses that specifically addressed the microbond test. Piggott[16] used shear-lag methods to evaluate the stresses and strain energy in pull-out specimens and microbond specimens. In our nomenclature, he assumed that the stresses in the fiber and matrix are

$$\sigma_{zz,1} = -\frac{\sigma_m V_2}{2V_1}(\phi_{es}(\zeta) + \phi_{os}(\zeta)) \quad \tau_{rz,1} = 0 \quad \sigma_{zz,2} = 0 \quad \tau_{rz,2} = -\frac{\sigma_m V_2}{4\xi V_2}(\phi_{es}'(\zeta) + \phi_{os}'(\zeta)) \tag{52}$$

As in our shear-lag analysis, all unspecified stresses are zero. Piggott's fiber stress, $\sigma_{zz,1}$, is identical to our shear-lag result in Equation (23) once it is realized the Piggott set $\sigma_0 = \sigma_f = 0$ and ignored thermal stresses ($\Delta T = 0$). The remaining stresses are different. Piggott assumed that the shear stresses in the fiber and the tensile stresses in the matrix make only negligible contributions to the total strain energy. The difference between his $\tau_{rz,2}$ and ours is a sign error in Piggott's result (which is irrelevant when calculating

energy) and a loss of the term linear in ξ (which is a consequence of stress equilibrium and the assumption that $\sigma_{zz,2} = 0$).

Evaluating the strain energy in the microbond specimen using the above stress state, Piggott found[16]

$$U_s(\rho) = 2\rho\pi r_1^2 \left\{ \left(\frac{\sigma_m V_2}{2V_1} \right)^2 \frac{1}{2E_A} \frac{2\coth 2\omega\rho}{\omega\rho} \right\} \tag{53}$$

This result agrees with our result in Equation (28) if we set $\Delta T = 0$, $C_{33s} = 1/(2E_A)$, and $C_{55} = 0$. The constants change because of the different stress state, in particular because of the assumption that $\tau_{rz,1} = \sigma_{zz,2} = 0$.

Comparing Equation (53) with Equation (28) when $\Delta T = 0$, we find that the two only agree when V_1 is vanishingly small. For pull-out specimens with small V_1, which was one of the intents of Piggott's analysis,[16] the strain energy in Equation (53) will be a reasonable approximation. For microbond specimens, where V_1 is larger then for pull-out specimens, or for $\Delta T \neq 0$, Equation (53) becomes a poor approximation. For typical microbond specimens and typical values of ΔT, Equations (28) and (53) differ by at least 50% and by as much as 800%. The conclusion is that it is a poor approximation to set $\tau_{rz,1} = \sigma_{zz,2} = 0$. Fortunately, it is straightforward to include them in a shear-lag analysis.

For predicting failure, Piggott assumed droplet debonding would occur when the total strain energy per unit interfacial area ($G_i = U_s/(2\pi r_1 l)$) becomes equal to G_{ic}[16]. The debonding stress is then predicted to be

$$\sigma_d = 2\sqrt{\frac{2G_{ic}E_A\omega\rho \tanh 2\omega\rho}{r_1}} \tag{54}$$

A similar total energy release model was also discussed in Ref. 8. This failure criterion is not a fracture mechanics criterion. Our experience with experimental results is that it does a poor job of predicting debond stress as a function of ρ. It predicts a smaller change in σ_d with ρ than is experimentally observed.[9]

Penn and Lee[17] attempted to improve on Piggott's analysis by using a true fracture mechanics failure criterion. As in Figure 4, they introduced a cracked region. For region I, they assumed a simpler stress state of

$$\sigma_{zz,1} = -\frac{\sigma_m V_2}{V_1} \quad \text{and} \quad \sigma_{zz,2} = 0 \tag{55}$$

This stress state follows Piggott's approach of neglecting the tensile stresses in the matrix. Their region I strain energy is

$$U_I(\delta) = \frac{2\delta\pi r_1^3 \sigma_d^2}{2E_A} \tag{56}$$

which is identical to Equation (32) if C_{33s} is replaced by $1/(2E_A)$. For region II, Penn and Lee used Piggott's stress state but accounted for the shorter droplet of axial ratio $\rho - \delta$. For energy release rate analysis, they used

$$G_i = \frac{\partial U_I(\delta)}{\partial A} + \frac{\partial U_s(\rho - \delta)}{\partial A} \tag{57}$$

This equation differs from the correct equation in Equation (34) in two ways. First, they ignored the contribution of external work to G_i. Like our analysis, they assumed the knife edges gripping the specimen were fixed. They perhaps then incorrectly assumed fixed grips meant no external work. Any specimen, however, must be gripped in two places. For the microbond specimen the knife edges grip the matrix and the second grip pulls the fiber. The second grip is not fixed and the external work done by displacement of the second grip must be included. Another difference between Equations (34) and (57) is the sign on the strain energy derivative. The proper definition of energy release rate has a negative sign, even under fixed-grip conditions.[19] Using Equation (57) and the simplified shear-lag stress state, Penn and Lee found the energy release rate to be[17]

$$G_{is}(0) = \frac{r_1}{2}\left\{\frac{\sigma_d^2}{2E_A}(1 + \operatorname{csch}^2 2\omega\rho)\right\} \tag{58}$$

Like Piggott's analysis, this equation agrees with Equation (40) if we set $\Delta T = 0$, $C_{33s} = 1/(2E_A)$, $C_{55s} = 0$, and correct the sign error on the $\operatorname{csch}^2 2\omega\rho$ term. We do not need to correct the sign on the first term because, coincidentally, the neglected work term, $\partial W/\partial A$, is equal to $2\partial U_1/\partial A$. The predicted debond force becomes

$$\sigma_d = \sqrt{\frac{4G_{ic}E_A \tanh^2 2\omega\rho}{r_1}} \tag{59}$$

In the limit as $\rho \to \infty$, the debond force is predicted to be

$$\sigma_d = \sqrt{\frac{4G_{ic}E_A}{r_1}} \tag{60}$$

which agrees with Equation (51) if $\Delta T = 0$ and $C_{33s} = 1/(2E_A)$.

Figure 5 also plots $G_i(0)$ as calculated by Piggott's analysis[16] and by Penn and Lee's analysis.[17] Both results differ significantly from our analyses and from the finite element calculations. Most of the discrepancy can be attributed to using $1/(2E_A)$ instead of C_{33s}. For typical volume fractions used in microbond tests, these two terms differ significantly. In summary, our new shear-lag analysis differs from previous shear-lag analyses in two important ways. First, our analysis includes residual thermal stresses. Second, our analysis includes shear stresses in the fiber and tensile stresses in the matrix. These stresses are easy to include and we found that they are not negligible for typical microbond specimens.

4 RESULTS

To generate a representative set of data, several fiber types were tested and the microdrop size (length and diameter) was varied among the samples. Each sample's droplet length and diameter were recorded prior to debonding (see Fig. 2). Only axisymmetric droplets were tested. The debond event was monitored through a telescope positioned near the test sample, and three possible outcomes were noted: partial debond, droplet shatter, and complete debond. Only the results from complete debonds were used. The sample preparation and testing procedures are described in more detail by Scheer.[9] Although there was much scatter in the individual data points, a simple smoothing routine can be applied to the data points. We smoothed the data by

averaging the debond force data over 20 μm increments of length. The smoothed debond force data as a function of droplet length are plotted in Figure 7 and 8 for both our 21 μm diameter E-glass fibers and Tesoro's Kevlar 49® data.[2] The error bars on the experiment data points are the standard deviation of the raw data points within the 20 μm range of smoothed data.

The example energy release rate in Figure 5 shows that at constant V_1, $G_i(0)$ increases as ρ increases. This result suggests that debond force should *decrease* as ρ increases. This prediction, however, is a contradiction of all experimental results as a function of ρ.[1-7] The problem is that in real experiments, V_1 is not a constant, but is a function of ρ. Because energy release rate and debond stress depend on V_1 and not just on ρ, it is insufficient to follow the standard practice of recording only droplet length and debond force.[1-7] To do an energy release rate analysis, we must also record V_1 as a function of droplet length.

We calculated V_1 and V_2 from the measured droplet diameter (D) and length (l). The droplet/fiber region of the specimen was assumed to be a ellipsoid of revolution with total volume:

$$V = \frac{4\pi}{3}\left(\frac{D}{2}\right)^2\left(\frac{l}{2}\right) \tag{61}$$

The volume fraction of the fiber is then

$$V_1 = \frac{\pi r_1^2 l}{V} = 1.5\left(\frac{r_1}{r_2}\right)^2 \tag{62}$$

where r_2 is the radius of the droplet. We recorded droplet diameters for each specimen but, for theoretical predictions, it is preferable to have a relation between diameter and length. A plot of droplet diameter as a function of length for one of the systems tested (a 21 μm diameter E-glass fiber with EPON 828 droplets) is shown in Figure 6. These data were fit to a line

$$D(l) = Al + B \tag{63}$$

As seen in Figure 6, the fit is excellent over the entire range of experimental results. The linear relation, however, is only expected to be valid when $D \gg 2r_1$, because it is

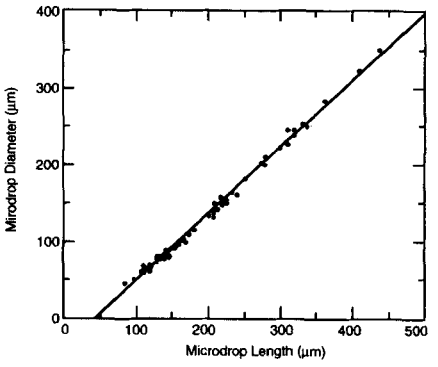

FIGURE 6 Plot of droplet diameter as a function of droplet length data for EPON 828 droplets on E-glass fibers of diameter 21 μm. The solid line is the best linear fit to the experimental data.

impossible for the droplet diameter to be less than the fiber diameter. In other words $D(l)$ will not continue to follow the line as l decreases, but instead will level off at $D \approx 2r_1$. There is some indication of $D(l)$ leveling off at the lowest l values in Figure 6. As long as we restrict analysis to droplets within the range of experimental droplets, the linear relation provides an accurate measure of $D(l)$. A consequence of not being able to extrapolate $D(l)$ to small l is that our theoretical curves do not pass through the origin. If necessary, this artifact could be corrected by using a more complicated form of $D(l)$ that works for all l. The fitting results for linear $D(l)$ for both material systems analyzed in this paper are given in Table I.

Experimental results and theoretical predictions for debonding EPON 828 droplets off 21 μm E-glass fibers are shown in Figure 7. We fit the experimental results to five different theories–the variational mechanics analysis (Eq. (43)), the new shear-lag analysis (Eq. (43) using a_s, b_s, and c_s), the simple limiting analysis for samples with high ρ (Eq. (50)), Piggott's total energy model[16] (Eq. (54)), and Penn and Lee's shear-lag analysis[17] (Eq. (60)). The first three analysis methods all gave excellent fits and gave G_{ic} of 219 J/m^2, 223 J/m^2, and 222 J/m^2. The fact that the simple analysis works as well as the other two analyses indicates that all droplet lengths in these experimental data are in the large ρ range. Piggott's total energy model gives the worst result and a G_{ic} of 31 J/m^2. The poor fit when using a total energy failure criterion agrees with the poor results when using a similar failure criterion in Ref. 9. Penn and Lee's shear lag analysis also gives a poor fit and a G_{ic} of 76 J/m^2.

When comparing our three theories with Penn and Lee's equation, we see that the calculated G_{ic}'s are significantly different. A significant reason for the discrepancies in G_{ic}'s is because our analysis uses C_{33s} while Penn and Lee's analysis is equivalent to having C_{33s} set equal to $1/(2E_A)$. For the fiber volume fractions of our specimens, C_{33s} is considerable larger than $1/(2E_A)$; the fit to Penn and Lee's equation compensates for this discrepancy by using a significantly smaller G_{ic}. Although we do not know of any direct measure of G_{ic}, a value of 220 J/m^2 agrees almost exactly with another energy interpretation of failure at an E-glass/epoxy interface.[22] We thus claim that a G_{ic} of 220 J/m^2 is more in line with expectation for epoxy systems than the lower value of 76 J/m^2. Another problem with Penn and Lee's analysis is that it ignores residual thermal stresses. The consequences of ignoring thermal stresses depends on the level of

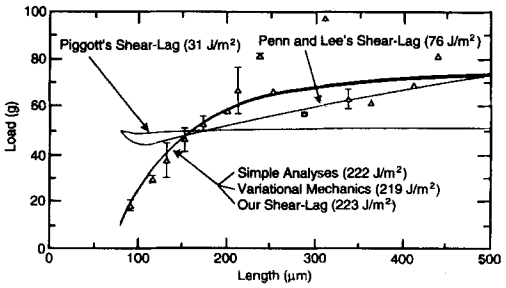

FIGURE 7 Plot of debond load *versus* microdrop length for debonding of EPON 828® droplets off 21 μm diameter E-glass fibers. The smooth lines are theoretical fits to the experiments using several different theories. The numbers next to each analysis description are the least squares values for G_{ic}.

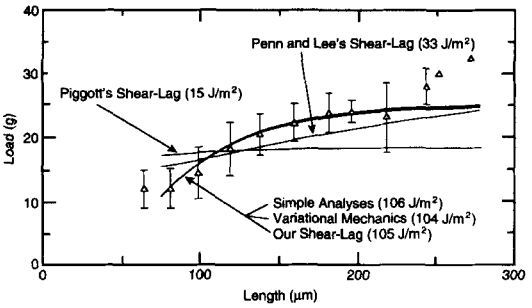

FIGURE 8 Plot of debond load *versus* microdrop length for debonding of EPON 828 droplets off Kevlar® 49 aramid fibers. The smooth lines are theoretical fits to the experiments using several different theories. The numbers next to each analysis description are the least squares values for G_{ic}.

ΔT. For the experiments in this paper, $\Delta T \approx -100\,^{\circ}\mathrm{C}$ and the thermal stresses contribute about 10% of the total energy release rate.

Experimental results and theoretical predictions for debonding EPON 828 droplets off Kevlar® 49 aramid fibers are shown in Figure 8. The experimental results in Figure 8 are from Ref. 2. Because that paper did not give the droplet diameter as a function of droplet length, we did some of our own experiments with EPON 828 droplets on Kevlar® 49 aramid fibers. The linear fit between $D(l)$ and l (see Table I) from our data was used to analyze the data in Figure 8. The variational mechanics analysis, our shear lag analysis, and the simple analysis gave G_{ic} of 104 J/m^2, 105 J/m^2, and 106 J/m^2. The fact that the simple analysis works as well as the other two analyses indicates, again, that all droplet lengths in this experimental data are in the large ρ range. Piggott's total energy gave a G_{ic} of 15 J/m^2. Penn and Lee's shear lag analysis gave a G_{ic} of 33 J/m^2. The fits of these two models were worse than to the first three.

All the shear-lag equations depend on the shear-lag parameter ω. Most shear-lag analyses adopt the shear-lag parameter recommended by Cox[12] (see Eq. (41)). Cox, however, derived this shear-lag parameter for use with high fiber volume fraction composites (greater than 50%). It should not be expected to be applicable to low volume fraction conditions that exist in microbond test specimens, pull-out test specimens,[16,17,23-26] or fragmentation test specimens.[27-31] We might consider looking for improved fits by treating ω as an adjustable parameter. For our shear-lag analysis, we found that ω has no effect on the final G_{ic}. The reason is that all specimens are in the high ρ range and inspection of Equation (51) shows that in the limit of large ρ, σ_d is independent of ω. Varying ω has minor effects on the fits to Piggott's or Penn and Lee's equation, but does not lead to any significant improvement in fit.

5 DISCUSSION AND CONCLUSIONS

For both experimental data sets presented above, the variational mechanics analysis, the shear-lag analysis, and the simple limiting analysis all gave excellent results. The

process of fitting the theories to experimental results allows one to measure the interfacial toughness, G_{ic}. This toughness should be interpreted as a mode I toughness of the interface. Previous fracture mechanics analyses suffer from two problems–incomplete energy balance and failure to account for residual stresses. Our new analyses correct these problems and we claim they give a useful fracture mechanics interpretation of microbond tests.

The fact that the simple analysis works as well as the more complete analyses means that, for typical microbond specimens, the energy release rate is in the high ρ limit. In other words, the energy released comes from a change in length of region I and a loss of thermal stresses as region II gets smaller. The details of the complex stress state at the top of region II are irrelevant because they do not release much energy. The simple variational analysis depends only on D_3, C_{33}, D_{3s}, and C_{33s} (see Eq. (50)). The simple shear-lag analysis is even simpler and depends only on D_{3s} and C_{33s}. Importantly, the simple shear-lag analysis is independent of the shear lag parameter ω. Because the differences between Equations (50) and (51) are small, especially for larger values of ρ, we propose the shear-lag result as a simple and elegant tool for analyzing microbond test results. To repeat that equation in terms of debond force, F_d

$$F_d = \pi r_1^2 \left(\sqrt{\frac{2G_{ic}}{r_1 C_{33s}}} - \frac{D_{3s}\Delta T}{C_{33s}} \right) \tag{64}$$

This equation is no harder to use than the currently-used average shear stress criterion in Equation (30). An important difference, however, is that Equation (64) gives F_d as a function of fiber volume fraction V_1 (V_1 is in C_{33s}), while Equation (30) depends only on ρ. Our recommendation, therefore, is that when running microbond tests, one should record debond force, droplet length, *and* droplet diameter. Droplet diameter can be used to estimate V_1. Recording only debond force and droplet length is insufficient for a fracture mechanics analysis of the microbond test.

The fact that the simple analysis works well further implies that $G_i(\delta)$, which can be evaluated from Equation (38) with $\delta \neq 0$, is approximately independent of δ. A plot of the complete $G_i(\delta)$ as a function of δ for a typical microbond specimen shows that this approximation is correct. $G_i(\delta)$ is independent of debond length except when the debond gets near the end of the specimen. At this point $G_i(\delta)$ decreases, but the assumptions in the model also break down, making the calculation of $G_i(\delta)$ for $\delta \approx \rho$ unreliable. When energy release rate is independent of crack length, a crack that initiates will propagate until failure. Thus, a constant energy release rate implies that complete failure can be predicted by the conditions required to cause crack initiation. This observation supports our use of $G_i(0)$ for predicting complete debonding of the droplet from the fiber.

A concern when using Equation (64) is verifying that all experimental results are in the high ρ limit. We have not tried all possible specimen geometries, but Equation (64) appears to work for typical polymeric droplets on high-modulus fibers (*e.g.*, E-glass, Kevlar® aramid, and carbon fibers). If specimen dimensions or matrix and fiber mechanical properties are substantially changed from those analyzed in this paper, it is recommended that the applicability of Equation (64) be verified by comparing its predictions with the more detailed analysis in Equation (43). If the comparison shows

them to be similar, then Equation (64) can be used. If they are not similar, then the Equation (43) should be used instead.

A concern about all analyses in this paper is that we analyzed an *idealized* specimen of concentric cylinders instead of an actual specimen with an elliptical droplet. The idealized specimen was adopted to make the analysis tractable, but two results argue that its use is acceptable. First, Day[32] did finite element analyses of both the idealized geometry and a realistic elliptical droplet. He examined the interfacial shear stresses and found that they were virtually unaffected by the details of the droplet shape. Second, the effectiveness of the simple model demonstrates that a global analysis works. We expect that the idealized geometry does a good job of capturing the global strain energy in a microbond specimen.

Recent scanning wettability studies of fibers after the debonding process show that the fracture process is rarely a pure interfacial fracture.[6,7] Instead, it is common to see cohesive failure within the fiber, in which case a small amount of the surface of the fiber is removed, or cohesive failure within the matrix, in which case a small amount of matrix remains on the fiber. These observations might seem to invalidate the analysis of this paper which assumes an interfacial fracture, but actually they do not. Consider analyzing experiments which all fail by the type of matrix cohesive fracture observed in Ref. 6. The matrix left on the fiber affects the stress analysis in region I (see Fig. 4). The fiber part of region I should be slightly larger and have different mechanical properties while the matrix part should be slightly smaller. The amount of matrix left on the fiber, however, is exceedingly small; it is beyond the resolution of scanning electron microscopy.[6] Thus, the effect of the matrix left on the fiber on the strain energy in region I will be negligible. The failure mode also has no effect on the strain energy in region II because the interface in that region is still intact. We finally conclude that the energy release rates calculated in this paper are valid for any failure mode as long as the amount of matrix left on the fiber during matrix cohesive failure or the amount of fiber removed during fiber cohesive failure is small.

Although our energy release rates and methods for determining G_{ic} are valid, the interpretion of G_{ic} is profoundly affected by failure mode. G_{ic} is only an *interfacial* toughness when the failure mode is at the interface. Matrix failures and fiber failures require reinterpreting G_{ic} as either a matrix cohesive toughness or a fiber cohesive toughness. Microbond tests should, therefore, always be supported by careful observation of the failure process by techniques such as scanning wettability.[6]

Acknowledgements

This work was supported by a grant from the Mechanics of Materials program at NSF (CMS-9401772), by a contract from NASA Langley Research Center (NASI-18833) monitored by Dr. John Crews, and by a gift from the Fibers Department of E. I. duPont deNemours & Company monitored by Dr. Alan R. Wedgewood. Additionally, R. J. Scheer was supported by an NSF graduate fellowship and a University of Utah research fellowship.

References

1. B. Miller, P. Muri and L. Rebenfeld, *Comp. Sci & Tech.* **28,** 17 (1987).
2. G. C. Tesoro, R. Benrashid, L. Rebenfeld and U. Gaur, *International Symposium on Polymers for Advanced Technologies*, 773, Jerusalem, Israel, August 17–21, 1987.

3. R. A. Haaksma and M. J. Cehelnik, *Mat. Res. Soc. Symp. Proc.* **170,** 71 (1990).
4. V. Rao, P. Herrera-Franco, A. D. Ozzello and L. T. Drzal, *J. Adhesion* **34,** 65 (1991).
5. H. D. Wagner, H. E. Gallis and E. Wiesel, *J. Mat. Sci.* **28,** 2238 (1993).
6. C. T. Chou, U. Gaur and B. Miller, *Comp. Sci & Tech.* **48,** 307 (1993).
7. C. T. Chou, U. Gaur and B. Miller, *J. Adhesion* **40,** 245 (1993).
8. R. J. Scheer and J. A. Nairn, *Composites Engineering* **2,** 641 (1992).
9. R. J. Scheer, "Application of a Variational Mechanics Stress Analysis and Energy Based Failure Criteria to the Microdrop Debond Test for Evaluation of the Adhesion Quality of Several Fiber-Matrix Systems," PhD Thesis, University of Utah, 1993.
10. H. Lee and K. Neville, *Handbook of Epoxy Resins* (McGraw-Hill, New York, 1967), p. 8–2.
11. J. A. Nairn, *Mech. of Materials* **13,** 131 (1992).
12. H. L. Cox, *Brit. J. Appl. Phys.* **3,** 72 (1952).
13. J. K. Kim, C. Baillie and Y. M. Mai, *J. Mat. Sci.* **27,** 3143 (1991).
14. L. M. Zhou, J. K. Kim and Y. M. Mai, *J. Mat. Sci.* **27,** 3155 (1992).
15. C. H. Hseuh, *Mat. Sci. and Eng.* **A154,** 125 (1992).
16. M. R. Piggott, *Comp. Sci. & Tech.* **30,** 295 (1987).
17. L. S. Penn and S. M. Lee, *J. Comp. Tech. & Res.* **11,** 23 (1989).
18. R. J. Day and M. Marquez, in *International Phenomena in Composite Materials*, I. Verpoest and F. R. Jones, Eds. (Butterworth-Heinemann Ltd., Oxford, England, 1991), p. 65.
19. J. G. Williams, *Fracture Mechanics of Polymers* (John Wiley & Sons, New York, 1984), p. 24.
20. M. L. Williams, *Bull. of the Seismological Society of America* **49,** 199 (1959).
21. Y. C. Gau, Y. M. Mai and B. Cotterell, *J. Appl. Math. and Phys.* **39,** 550 (1988).
22. A. T. DiBenedetto, *Comp. Sci & Tech.* **42,** 103 (1991).
23. L. S. Penn and E. R. Bowler, *Surf. Interf. Anal.* **3,** 161 (1981).
24. L. S. Penn, F. A. Bystry and H. J. Marchionni, *Polym. Comp.* **4,** 26 (1983).
25. M. R. Piggott, P. S. Chua and D. Andison, *Polym. Comp.* **6,** 242 (1985).
26. M. R. Piggott and S. R. Dai, *Comp. Sci. & Tech.* **31,** 15 (1988).
27. N. J. Wadsworth and I. Spilling, *Br. J. Appl. Phys. (J. Phys. D.)* **1,** 1049 (1968).
28. A. A. Fraser, F. H. Ancker and A. T. DiBenedetto, *Proc. 30th Conf. SPI Reinforced Plastics Div.* **Section 22-A,** 1 (1975).
29. W. A. Fraser, F. H. Ancker, A. T. DiBenedetto and B. Elbirli, *Polym. Comp.* **4,** 238 (1983).
30. L. T. Drzal, M. J. Rich and P. F. Lloyd, *J. Adhesion* **16,** 1 (1983).
31. W. D. Bascom and R. M. Jensen, *J. Adhesion* **19,** 219 (1986).
32. R. J. Day, *Proc. of the Second Conf. on Deformation and Fracture of Composites*, Manchester, UK, March 1993.

APPENDIX

In the variational mechanics analysis, the stresses and energy release rate were expressed in terms of constants that depend on the sample dimensions and on the mechanical properties of the fiber and the matrix:

$$A_0 = \frac{V_2(1-\nu_T)}{V_1 E_T} + \frac{1-\nu_m}{E_m} + \frac{1+\nu_m}{V_1 E_m} \tag{65}$$

$$A_1 = \left(\frac{1-\nu_T}{E_T} - \frac{1-\nu_m}{E_m}\right)(1+\nu_m)\left(1 + \frac{2\ln V_1}{V_2}\right) + \frac{2(1-\nu_m)}{V_2 E_m} \tag{66}$$

$$A_2 = \frac{1-\nu_T}{E_T} - \frac{1-\nu_m}{E_m} \tag{67}$$

$$A_3 = -\left(\frac{\nu_A}{E_A} + \frac{V_1 \nu_m}{V_2 E_m}\right) \tag{68}$$

$$A_4 = \frac{\nu_m}{V_2 E_m} \tag{69}$$

$$A_5 = \alpha_T - \alpha_m \tag{70}$$

$$C_{33} = \frac{1}{2}\left(\frac{1}{E_A} + \frac{V_1}{V_2 E_m}\right) - \frac{V_2 A_3^2}{V_1 A_0} \tag{71}$$

$$C_{35} = \frac{1}{16}\left[A_3\left[(1+\nu_m)\left(1 + \frac{2\ln V_1}{V_2}\right) - \frac{V_2 A_1}{V_1 A_0}\right] - 2A_4\right] \tag{72}$$

$$\begin{aligned} C_{55} = \frac{1}{256}\Bigg\{ & \frac{1-\nu_T}{E_T}\left[\frac{5+2\nu_T}{3} + \nu_m(2+\nu_m)\right] + \frac{4A_2(1+\nu_m)^2 \ln V_1}{V_2}\left(1 + \frac{\ln V_1}{V_2}\right) - \frac{V_2 A_1^2}{V_2 A_0} \\ & + \frac{1-\nu_m}{E_m}\left[\frac{V_2^2(1+\nu_m)(5+3\nu_m) - 3V_2(1+\nu_m)(3+\nu_m) + 6(5+3\nu_m)}{3V_1 V_2}\right. \\ & \left. + \frac{8(1+\nu_m)\ln V_1}{V_2^2}\right]\Bigg\} \end{aligned} \tag{73}$$

$$C_{44} = \frac{1}{16}\left[\frac{1}{G_A} - \frac{1}{G_m}\left(1 + \frac{2}{V_2} + \frac{2\ln V_1}{V_2^2}\right)\right] \tag{74}$$

$$C_{13} = -\frac{1}{2V_2 E_m} - \frac{V_2 A_3 A_4}{V_1 A_0} \tag{75}$$

$$C_{11} = \frac{1}{2V_1 V_2 E_m} - \frac{V_2 A_4^2}{V_1 A_0} \tag{76}$$

$$D_3 = -\frac{V_2 A_3}{V_1 A_0}[\alpha_T - \alpha_m] + \frac{1}{2}[\alpha_A - \alpha_m] \tag{77}$$

In these equations, E_A and E_T are the axial and transverse tensile moduli of the fiber, G_A is the axial shear modulus of the fiber, ν_A and ν_T are the axial and transverse Poisson's ratios of the fiber, α_A and α_T are the axial and transverse thermal expansion coefficients of the fiber, and E_m, G_m, ν_m, and α_m are the tensile modulus, shear modulus, Poisson's ratio, and thermal expansion coefficient of the matrix. (Note: the expression of C_{35} corrects misprints in both Refs. 8 and 11).

The constants p and q are

$$p = \frac{2C_{35} - C_{44}}{C_{55}} \quad \text{and} \quad q = \frac{C_{33}}{C_{55}} \tag{78}$$

The functions $\dot{\phi}_e(\zeta)$ and $\phi_0(\zeta)$ depend on the values of p and q. When $p^2 - 4q < 0$

$$\phi_e(\zeta) = \frac{2h_2'(\rho)\cosh\alpha\zeta\cos\beta\zeta - 2h_1'(\rho)\sinh\alpha\zeta\sin\beta\zeta}{\beta\sinh 2\alpha\rho + \alpha\sin 2\beta\rho} \tag{79}$$

$$\phi_0(\zeta) = \frac{2h_4'(\rho)\sinh\alpha\zeta\cos\beta\zeta - 2h_3'(\rho)\cosh\alpha\zeta\sin\beta\zeta}{\beta\sinh 2\alpha\rho - \alpha\sin 2\beta\rho} \tag{80}$$

where

$$h_1(\rho)=\cosh\alpha\rho\cos\beta\rho \quad h_3(\rho)=\sinh\alpha\rho\cos\beta\rho \quad \alpha=\tfrac{1}{2}\sqrt{2\sqrt{q}-p}$$
$$h_2(\rho)=\sinh\alpha\rho\sin\beta\rho \quad h_4(\rho)=\cosh\alpha\rho\sin\beta\rho \quad \beta=\tfrac{1}{2}\sqrt{2\sqrt{q}+p} \tag{81}$$

and $h_i'(\rho)$ is the derivative of $h_i(\rho)$ with respect to ρ. When $p^2-4q>0$

$$\phi_e(\zeta)=\frac{\beta\cosh\alpha\zeta\,\operatorname{csch}\alpha\rho-\alpha\cosh\beta\zeta\,\operatorname{csch}\beta\rho}{\beta\coth\alpha\rho-\alpha\coth\beta\rho} \tag{82}$$

$$\phi_0(\zeta)=\frac{\beta\sinh\alpha\zeta\,\operatorname{sech}\alpha\rho-\alpha\sinh\beta\zeta\,\operatorname{sech}\beta\rho}{\beta\tanh\alpha\rho-\alpha\tan\beta\rho} \tag{83}$$

where

$$\alpha=\sqrt{-\frac{p}{2}+\sqrt{\frac{p^2}{4}-q}} \quad \beta=\sqrt{-\frac{p}{2}-\sqrt{\frac{p^2}{4}-q}} \tag{84}$$

For strain energy and energy release rate, the functions $\chi_e(\rho)$ and $\chi_0(\rho)$, and their derivatives, have the following explicit forms. When $p^2-4q<0$

$$\chi_e(\rho)=2\alpha\beta(\alpha^2+\beta^2)\frac{\cosh 2\alpha\rho-\cos 2\beta\rho}{\beta\sinh 2\alpha\rho+\alpha\sin 2\beta\rho} \tag{85}$$

$$\chi_0(\rho)=2\alpha\beta(\alpha^2+\beta^2)\frac{\cosh 2\alpha\rho+\cos 2\beta\rho}{\beta\sinh 2\alpha\rho-\alpha\sin 2\beta\rho} \tag{86}$$

$$\chi_e'(\rho)=4\alpha\beta(\alpha^2+\beta^2)^2\frac{\sinh 2\alpha\rho\sin 2\beta\rho}{(\beta\sinh 2\alpha\rho+\alpha\sin 2\beta\rho)^2} \tag{87}$$

$$\chi_0'(\rho)=-4\alpha\beta(\alpha^2+\beta^2)^2\frac{\sinh 2\alpha\rho\sin 2\beta\rho}{(\beta\sinh 2\alpha\rho-\alpha\sin 2\beta\rho)^2} \tag{88}$$

When $p^2-4q>0$

$$\chi_e(\rho)=\alpha\beta(\beta^2-\alpha^2)\frac{1}{\beta\coth\alpha\rho-\alpha\coth\beta\rho} \tag{89}$$

$$\chi_0(\rho)=\alpha\beta(\beta^2-\alpha^2)\frac{1}{\beta\tanh\alpha\rho-\alpha\tanh\beta\rho} \tag{90}$$

$$\chi_e'(\rho)=\alpha^2\beta^2(\beta^2-\alpha^2)\frac{\operatorname{csch}^2\alpha\rho-\operatorname{csch}^2\beta\rho}{(\beta\coth\alpha\rho-\alpha\coth\beta\rho)^2} \tag{91}$$

$$\chi_0'(\rho)=-\alpha^2\beta^2(\beta^2+\alpha^2)\frac{\operatorname{sech}^2\alpha\rho-\operatorname{sech}^2\beta\rho}{(\beta\tanh\alpha\rho-\alpha\tanh\beta\rho)^2} \tag{92}$$

Note that these equations for $\chi_e'(\rho)$ and $\chi_0'(\rho)$ correct misprints in Ref. 8.

In the shear-lag analysis, the stresses and energy release rates were expressed in terms of constants that depend on the sample dimensions and on the mechanical properties of

the fiber and the matrix:

$$C_{13s} = -\frac{1}{2V_2E_m} \tag{93}$$

$$C_{33s} = \frac{1}{2}\left(\frac{1}{E_A} + \frac{V_1}{V_2E_m}\right) \tag{94}$$

$$C_{55s} = \omega^2 C_{44} - C_{33s} \tag{95}$$

$$D_{3s} = \frac{1}{2}(\alpha_A - \alpha_m) \tag{96}$$

The functions used to define the stress are

$$\phi_{es}(\zeta) = \frac{\cosh\omega\zeta}{\cosh\omega\rho} \quad \text{and} \quad \phi_{0s}(\zeta) = \frac{\sinh\omega\zeta}{\sinh\omega\rho} \tag{97}$$

The functions used to define the strain energy are

$$\chi_a(\rho) = \frac{1}{2}\left(\frac{\tanh\omega\rho}{\omega} - \rho\,\mathrm{sech}^2\omega\rho\right) \tag{98}$$

$$\chi_a''(\rho) = \omega\rho\,\mathrm{sech}^2\,\omega\rho\tanh\omega\rho \tag{99}$$

$$\chi_b(\rho) = \frac{1}{2}\left(\frac{\coth\omega\rho}{\omega} + \rho\,\mathrm{csch}^2\omega\rho\right) \tag{100}$$

$$\chi_b''(\rho) = -\omega\rho\,\mathrm{csch}^2\,\omega\rho\coth\omega\rho \tag{101}$$